Reviews of Electromagnetics, Vol. IV, 2025
EuCAP 2025 Special Issue
DOI: 10.53792/RoE/2025/25012

Reviews of Electromagnetics
EuCAP 2025 Special Issue

Scan Limitations of Open-ended Ridged Waveguide Apertures for Ka-band Satellite Communication Applications

Sören Harms[1,2,3]*, Jean-Philippe Fraysse[1], Alessandro Garufo[2], Ulf Johannsen[3], Stefania Monni[2,3]

Abstract
Open-ended ridged waveguide phased array antennas are of high interest for low Earth orbit satellite communication applications due to their high efficiencies and power handling capacities. This paper analyzes the scan limitations with respect to active matching, axial ratio (AR), and realized gain of circular and hexagonal waveguide apertures with three and six ridges for a Ka-band satellite downlink application. Strong degradation of the active reflection coefficient (ARC), the coupling coefficient to the terminated (cross-polarized) port of a polarizer, the AR, and the realized gain are observed at high scan angles and frequencies when using a large element periodicity near the grating lobe threshold. For the open-ended hexagonal six-ridged waveguide, the scan limitations are investigated in detail for several element periodicities. The degradations can be related to three conditions. First, the onset of higher-order Floquet modes leads to single-mode scan blindness associated with one of the two orthogonal fundamental waveguide modes. Second, a transmission zero of one of the two fundamental waveguide modes far outside the operational band, occurring when the phase constants of the fundamental waveguide modes align with those of the fundamental Floquet modes, is interpreted as surface wave propagation and results in an increased attenuation of the affected fundamental waveguide mode at the maximum operational frequency. Third, the onset of higher-order waveguide modes induces modal coupling between the fundamental and the first two higher-order waveguide modes. Each of these conditions results in unequal contributions from the two fundamental waveguide modes to the radiated field, thereby degrading the overall performance. These scan limitations can be mitigated by using open-ended ridged waveguides with an electrically short evanescent end-section, allowing for large element periodicities while meeting the AR requirements for Ka-band satellite communication applications.

Key terms
Phased array antenna; ridged waveguides; floquet modes; scan blindness; surface wave propagation; evanescent; satellite communication; Ka-band; low earth orbit

[1] *Thales Alenia Space, Toulouse, France*
[2] *TNO Defense, Safety, and Security, Den Haag, The Netherlands*
[3] *Eindhoven University of Technology, Eindhoven, The Netherlands*
***Corresponding author**: s.harms@tue.nl

Received: 23/05/2025, Accepted: 20/11/2025, Published: 28/11/2025

1. Introduction

In current 6G communication architectures, it is foreseen that non-terrestrial networks (NTNs) will be integrated with traditional terrestrial networks using large low Earth orbit (LEO) satellite constellations [1, 2]. Direct and indirect access schemes will improve user connectivity. While direct access will provide a direct user-to-satellite link using the L- and S-band, indirect access will provide high data rates accessible through base stations or very small aperture terminals (VSATs) using the Ka-band. Today, the Ka-band is already widely used in satellite communications, and with 3GPP Release 18, the frequency bands n512, n511, and n510 (downlink: 17.3 - 20.2 GHz, uplink: 27.5 - 30 GHz) have been added for use in NTNs [3].

For LEO satellite communications payloads, circularly polarized phased array antennas (PAAs) are essential building

blocks that provide wide-angle electronic beam steering with multiple high-gain beams. Waveguide antennas are widely used in satellite communications due to their high efficiency and power handling capabilities [4]. Recently, open-ended square, circular, and hexagonal ridged waveguide apertures using rectangular and triangular lattice configurations have been proposed [5]-[11]. In particular, [6] and [7] introduced a circular three-ridged choked horn aperture with spline-shaped ridge transitions, while [8] proposed a similar aperture using evanescent waveguide sections. Furthermore, in [10] we presented a hexagonal six-ridged slotted horn aperture with exponentially tapered wall openings and ridge decays.

Square, circular, and hexagonal waveguides support the propagation of two orthogonal fundamental modes that are required to achieve circular polarization. The ridges reduce the cut-off frequencies of the fundamental waveguide modes, allowing smaller waveguide dimensions while still meeting the bandwidth requirements. Maximizing the element periodicity in a PAA is essential to simplify radio frequency (RF) front-end integration, thermal management, and to minimize the number of antenna elements and control nodes. Triangular lattices are preferred over rectangular lattices because larger element periodicities can be realized for a grating lobe free operation. In addition, the larger tolerable element spacing supports waveguide propagation at lower frequencies. Advances in metal-based additive manufacturing enable the cost-effective realization of these PAAs for centimeter wave (cmW) and millimeter wave (mmW) frequencies [12]-[15].

As expected for flat panel PAAs, performance degradation of the active reflection coefficient (ARC) and axial ratio (AR) has been observed in the literature for open-ended ridged waveguide apertures when scanned far from the broadside [9]-[11]. This paper continues our discussion started in [11] on analyzing the scan limitations of such apertures for a Ka-band satellite downlink application. In particular, four element geometries are considered, consisting of circular and hexagonal waveguides with three and six ridges. The apertures are studied with respect to active matching, AR, and realized gain. For the hexagonal waveguide with six ridges, the scan limitations are analyzed in detail, including a modal analysis for several element periodicities. As an extension to [11], we also investigated open-ended ridged waveguides with an electrically short evanescent waveguide end-section to address the identified scan limitations. Finally, a comparison with similar ridged waveguide apertures reported in the literature is made.

2. Open-ended Ridged Waveguide Apertures

For a LEO Ka-band satellite downlink application, where satellites typically operate at altitudes between 600 and 1200 km, the transmitting PAA must operate from 17.3 - 20.2 GHz (relative bandwidth of 15.5%) with scan angles of up to $\pm 50^\circ$. Although the formation of grating lobes outside the satellite's field of view can be tolerated, strong degradation of the active matching and the AR has already been observed in the literature for element periodicities smaller than the maximum tolerable grating lobe free element periodicity [9]-[11]. Therefore, the apertures analyzed in the following are arranged to avoid grating lobes within the operational scan range ($\theta_0 \leq 50^\circ$) and the maximum operational frequency ($f_{max} = 20.2$ GHz). Consequently, the maximum grating lobe free element periodicity in a triangular lattice is about $0.65\lambda_{min}$ (≈ 9.65 mm).

Four geometries consisting of circular and hexagonal ridged waveguides are considered: a circular three-ridged waveguide (C3RWG), a circular six-ridged waveguide (C6RWG), a hexagonal three-ridged waveguide (H3RWG), and a hexagonal six-ridged waveguide (H6RWG). In Fig. 1 all four ridged waveguide geometries are depicted. The ridge height is the primary parameter that modulates the cut-off frequencies of the waveguide modes for a fixed waveguide size. Fig. 2 shows the cut-off frequencies of the two fundamental (denoted as waveguide mode 1/2) and first higher-order waveguide modes (denoted as waveguide mode 3/4) as functions of the ridge height for a fixed ridge width of $0.034\lambda_{min}$ ($= 0.5$ mm) and an element periodicity of $0.65\lambda_{min}$ with a minimum waveguide wall thickness of $0.027\lambda_{min}$ ($= 0.4$ mm). Waveguides with three ridges have a significantly larger fundamental mode bandwidth than those with six ridges. Among the three-ridged waveguides, the circular geometry provides the largest bandwidth, whereas among the six-ridged waveguides, the hexagonal geometry provides the largest bandwidth. Nevertheless, all four ridged waveguide geometries are able to cover the Ka-band satellite downlink band. In the following, the ridge heights are selected for identical fundamental mode cut-off frequencies of approximately 16.5 GHz, providing some margin to the minimum operational frequency ($f_{min} = 17.3$ GHz).

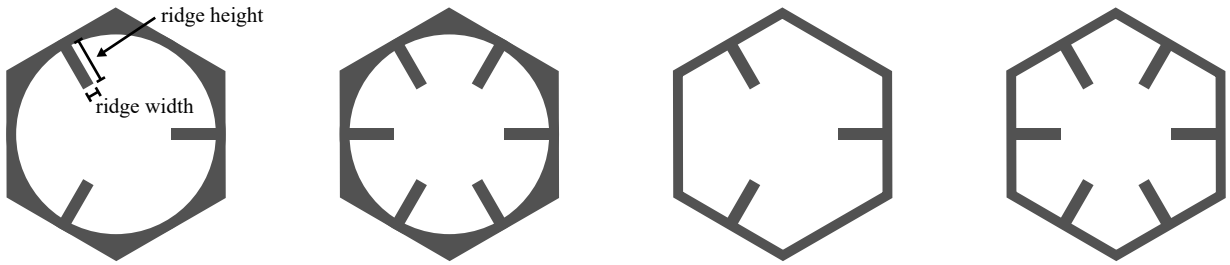

(a) C3RWG **(b)** C6RWG **(c)** H3RWG **(d)** H6RWG

Figure 1: Considered waveguide geometries: (a) circular three-ridged waveguide (C3RWG), (b) circular six-ridged waveguide (C6RWG), (c) hexagonal three-ridged waveguide (H3RWG), and (d) hexagonal six-ridged waveguide (H6RWG).

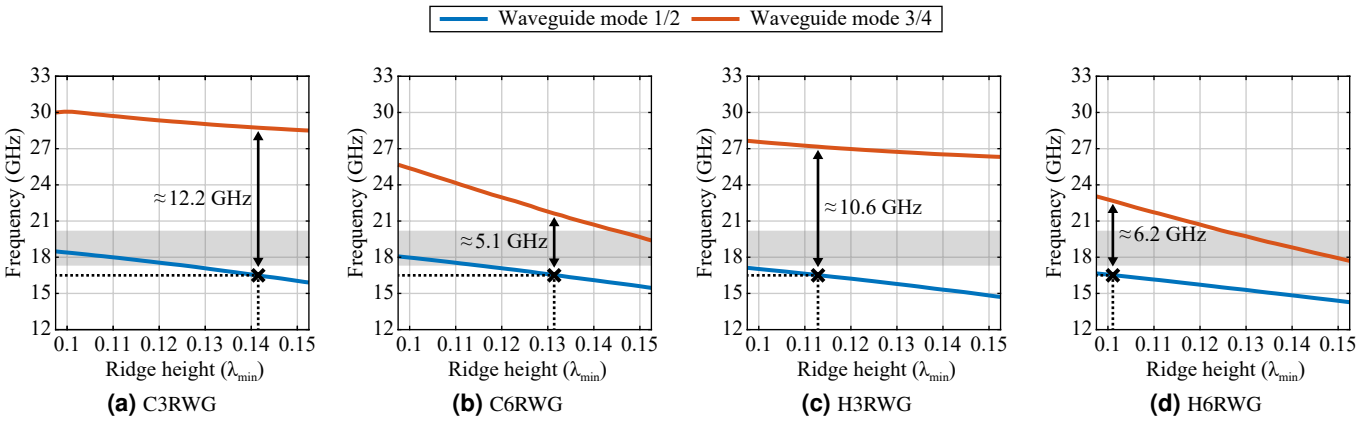

Figure 2: Cut-off frequencies of the fundamental (denoted as waveguide mode 1/2) and first higher-order waveguide modes (denoted as waveguide mode 3/4) as functions of the ridge height for the four considered waveguide geometries with an element periodicity of $0.65\lambda_{\text{min}}$. A black cross marks the ridge heights chosen for fundamental mode cut-off frequencies of 16.5 GHz.

2.1. Scan Limitations

The scan limitations of all four waveguide geometries are analyzed. The apertures are modeled as perfect electric conductors and simulated using an ideal excitation of the waveguide modes in an infinite array environment in Ansys HFSS [16]. Fig. 3 illustrates an infinite ridged waveguide PAA aperture scanning in the (ϕ_0, θ_0) - direction with respect to the used reference coordinate system.

Furthermore, the apertures are evaluated with an ideal polarizer that generates a perfectly circularly polarized excitation of the two orthogonal waveguide modes. Fig. 4 illustrates the circuit diagram of a ridged waveguide aperture cascaded with an ideal polarizer, similar to that in [5]. Depending on the selected port of the polarizer, either left-hand circular polarization (LHCP) or right-hand circular polarization (RHCP) is excited. Assuming RHCP in the following, the ARC at the excited (co-polarized) port of the polarizer can be represented as

$$\text{ARC}_{\text{RHCP}} = \frac{1}{2} \cdot \left(\text{S}_{11} - \text{S}_{22} + j \cdot (\text{S}_{12} + \text{S}_{21})\right) \tag{1}$$

and the coupling coefficient to the terminated (cross-polarized) port of the polarizer as

$$\text{C}_{\text{LHCP}} = \frac{1}{2} \cdot \left(\text{S}_{21} - \text{S}_{12} + j \cdot (\text{S}_{11} + \text{S}_{22})\right), \tag{2}$$

with S_{ii} and S_{ij} as the self and mutual coupling coefficients, respectively, of the two fundamental waveguide modes. Further, the electric field for LHCP and RHCP can be defined as

$$\text{E}_{\text{LHCP}} = \frac{1}{\sqrt{2}} \cdot \left(\text{E}_\theta - j \cdot \text{E}_\phi\right) \tag{3}$$

$$\text{E}_{\text{RHCP}} = \frac{1}{\sqrt{2}} \cdot \left(\text{E}_\theta + j \cdot \text{E}_\phi\right), \tag{4}$$

where E_θ and E_ϕ are the complex total electric field components in the far-field in a spherical coordinate system. The AR is calculated as

$$\text{AR} = \sqrt{\frac{|\text{E}_\theta|^2 + |\text{E}_\phi|^2 + |\text{E}_\theta^2 + \text{E}_\phi^2|}{|\text{E}_\theta|^2 + |\text{E}_\phi|^2 - |\text{E}_\theta^2 + \text{E}_\phi^2|}} \tag{5}$$

and the co-polarized (RHCP) realized gain as

$$\text{G}_{\text{RHCP}} = \frac{4\pi \cdot \text{U}_{\text{RHCP}}}{\text{P}_{\text{inc}}}, \tag{6}$$

with P_{inc} as the incident power and

$$\text{U}_{\text{RHCP}} = \frac{1}{2} \cdot \frac{|\text{E}_{\text{RHCP}}|^2}{\eta_0} \cdot \text{r}^2, \tag{7}$$

where η_0 is the free-space impedance and r is the distance from the antenna [17].

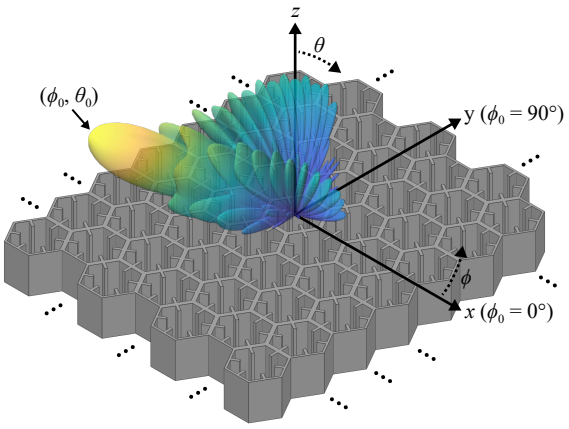

Figure 3: Illustration of an infinite ridged waveguide PAA aperture scanning in the (ϕ_0, θ_0) - direction with respect to the used reference coordinate system.

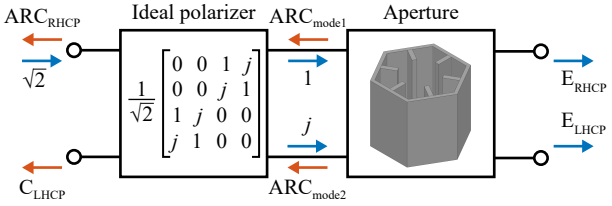

Figure 4: Circuit diagram of a ridged waveguide aperture cascaded with an ideal polarizer.

Fig. 5 shows the ARC, the coupling coefficient, and the AR of the waveguide apertures with an element periodicity of $0.65\lambda_{\text{min}}$ at the broadside and the maximum scan angle. As expected, while the waveguide elements with three ridges show symmetry in 120° sectors, the waveguide elements with six ridges show symmetry in 60° sectors. Moreover, waveguides with the same number of ridges exhibit similar behavior.

Although the ARCs and the coupling coefficients are typically less than -10 dB at broadside, the ARCs and the coupling coefficients degrade significantly with increasing frequency at high scan angles. For the three-ridged waveguides the ARCs and coupling coefficients peak at the maximum operational frequency around -5.5 dB and -3.5 dB, respectively, while for the six-ridged waveguides the ARCs and coupling coefficients peak

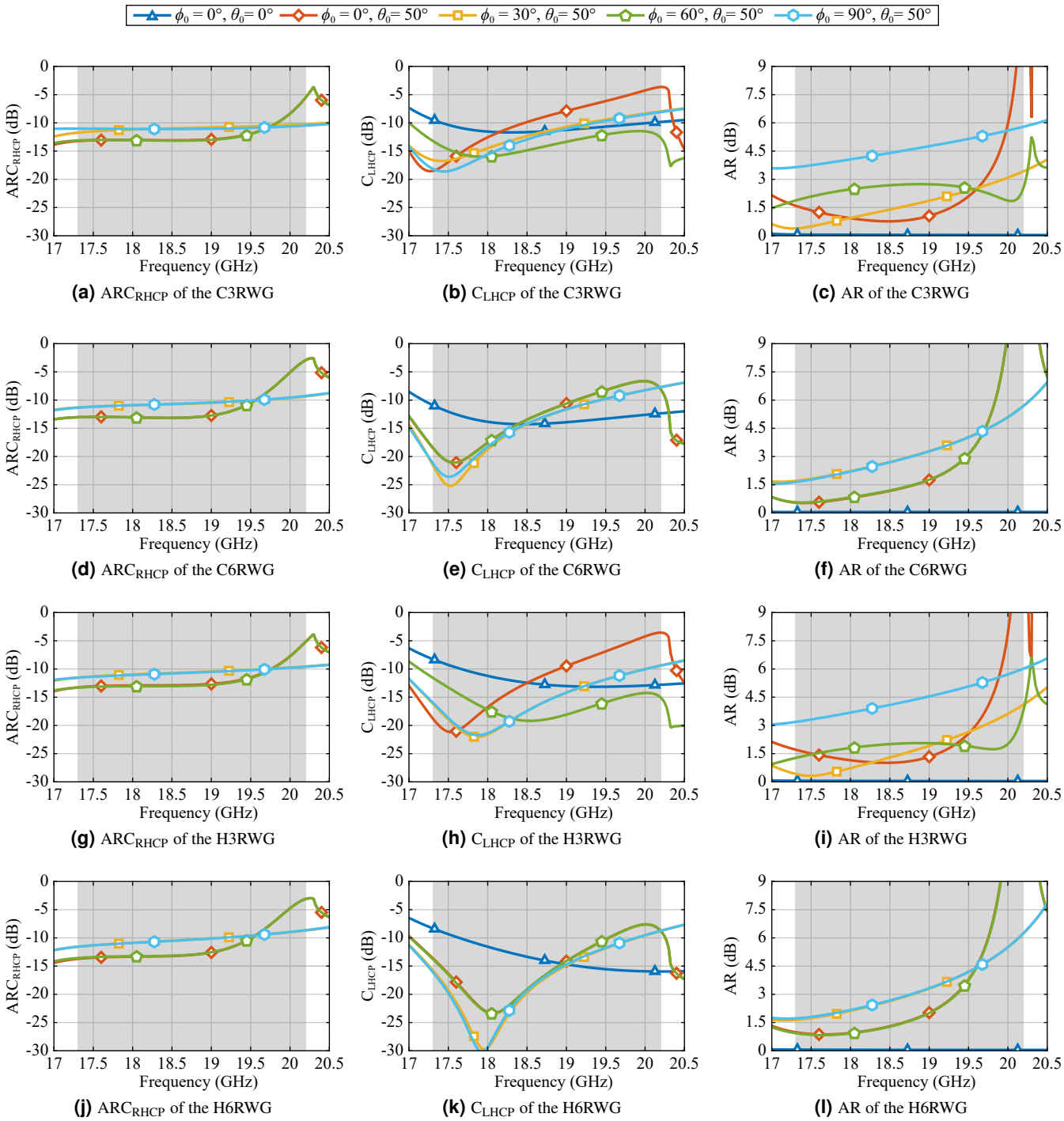

(a) ARC_{RHCP} of the C3RWG **(b)** C_{LHCP} of the C3RWG **(c)** AR of the C3RWG

(d) ARC_{RHCP} of the C6RWG **(e)** C_{LHCP} of the C6RWG **(f)** AR of the C6RWG

(g) ARC_{RHCP} of the H3RWG **(h)** C_{LHCP} of the H3RWG **(i)** AR of the H3RWG

(j) ARC_{RHCP} of the H6RWG **(k)** C_{LHCP} of the H6RWG **(l)** AR of the H6RWG

Figure 5: ARC, coupling coefficient, and AR as functions of frequency of the four considered waveguide apertures with element periodicities of $0.65\lambda_{\text{min}}$ (≈ 9.65 mm) at the broadside and at the maximum scan angle of $\theta_0 = 50°$ for $\phi_0 = 0°$, 30°, 60°, and 90°. The ridge dimensions are set accordingly for identical fundamental waveguide mode cut-off frequencies of 16.5 GHz. Some curves are hidden under others due to symmetry. The considered operational band is highlighted in light gray.

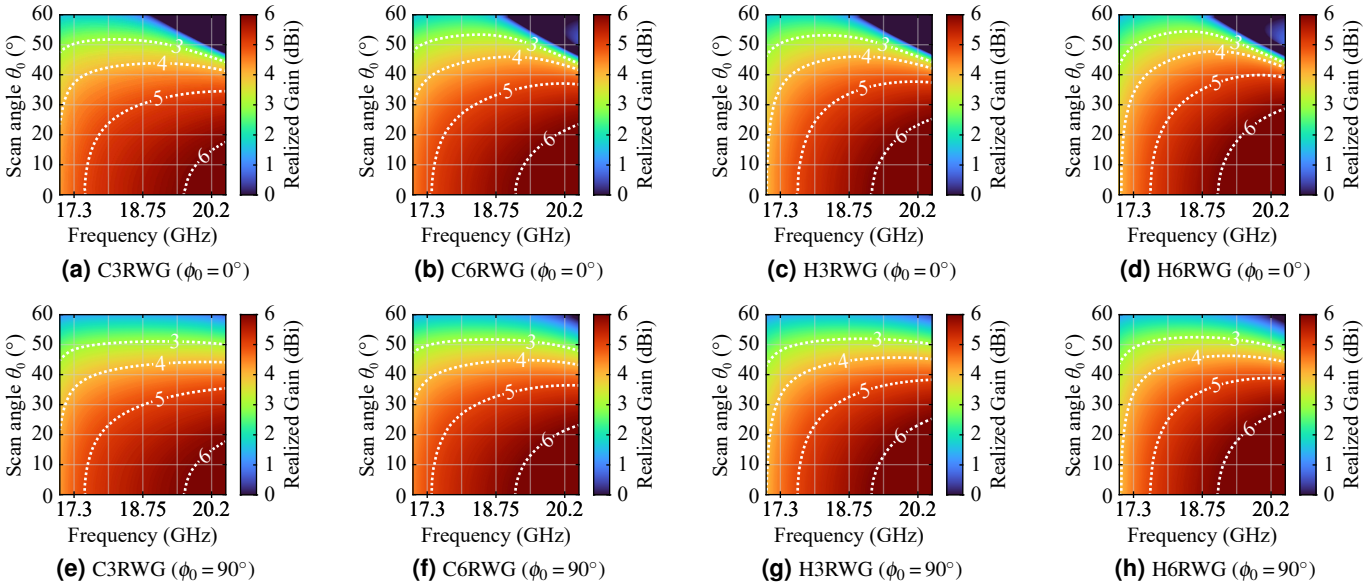

(a) C3RWG ($\phi_0 = 0°$) **(b)** C6RWG ($\phi_0 = 0°$) **(c)** H3RWG ($\phi_0 = 0°$) **(d)** H6RWG ($\phi_0 = 0°$)

(e) C3RWG ($\phi_0 = 90°$) **(f)** C6RWG ($\phi_0 = 90°$) **(g)** H3RWG ($\phi_0 = 90°$) **(h)** H6RWG ($\phi_0 = 90°$)

Figure 6: Co-polarized (RHCP) realized gain as a function of frequency and scan angle θ_0 of the four considered waveguide apertures with element periodicities of $0.65\lambda_{\text{min}}$ for $\phi_0 = 0°$ and 90°.

Table 1: Summary of the scan limitations of the four considered waveguide apertures with element periodicities of $0.65\lambda_{\text{min}}$.

Aperture	ARC_{RHCP}	C_{LHCP}	AR	$\text{G}^{\text{max}}_{\text{RHCP}}$	Scan loss
C3RWG	$\leq$ -5.5 dB	$\leq$ -3.6 dB	$\leq$ 17.5 dB	4.7 – 6.2 dBi	$\leq$ 8.8 dB
C6RWG	$\leq$ -2.9 dB	$\leq$ -6.6 dB	$\leq$ 38.1 dB	4.9 – 6.4 dBi	$\leq$ 9.4 dB
H3RWG	$\leq$ -5.2 dB	$\leq$ -3.5 dB	$\leq$ 25.4 dB	4.6 – 6.4 dBi	$\leq$ 11 dB
H6RWG	$\leq$ -3.1 dB	$\leq$ -7.6 dB	$\leq$ 51.2 dB	4.6 – 6.5 dBi	$\leq$ 9.1 dB

at the maximum operational frequency around -3 dB and -7 dB, respectively.

Similarly, a strong degradation of the AR can be observed for all elements. The $\phi_0 = 0°$- and the $\phi_0 = 90°$-planes can be identified as the two critical planes. In both ϕ-planes, a strong increase with frequency can be observed, exceeding the satellite communication specifications of 3 dB. For the six-ridged waveguides, in the $\phi_0 = 0°$-plane, the AR degrades slightly earlier than for the three-ridged waveguides. However, at $\phi_0 = 90°$, the AR of the three-ridged waveguides remains above 3 dB across the entire operational band.

In Fig. 6, the co-polarized (RHCP) realized gain is shown as a function of frequency and scan angle θ_0 for $\phi_0 = 0°$ and 90° for the four considered waveguide apertures with an element periodicity of $0.65\lambda_{\text{min}}$. For all elements the realized gain peaks roughly between 4.7 dBi and 6.4 dBi with frequency at broadside and decreases with scan angle θ_0. As was previously observed for the AR, a strong decrease of the realized gain of more than 9 dB can be also seen at the maximum operational frequency for $\phi_0 = 0°$, while for $\phi_0 = 90°$ the realized gain only drops by approximately 3.4 dB.

Table 1 summarizes the scan limitations of the four analyzed ridged waveguide apertures. Overall, the degradation at high frequencies and scan angles limits the performance of all elements.

2.2. Analysis of the Hexagonal Six-Ridged Waveguide

For conciseness, this paper will analyze the H6RWG in detail as an example, as it exhibits significant degradation in ARC, AR, and realized gain, while also allowing for simplified evaluation due to its 60° rotational symmetry. As a result, only two scan directions in the ϕ_0-plane are sufficient to characterize all scan

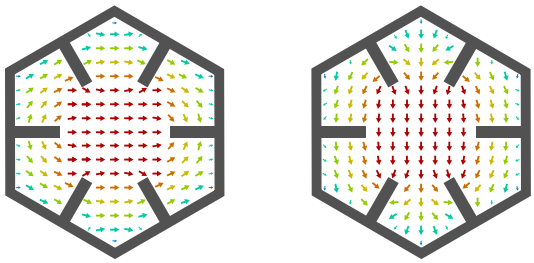

(a) Waveguide mode 1 **(b)** Waveguide mode 2

Figure 7: Illustrations of the two fundamental waveguide mode electric field distributions of the H6RWG.

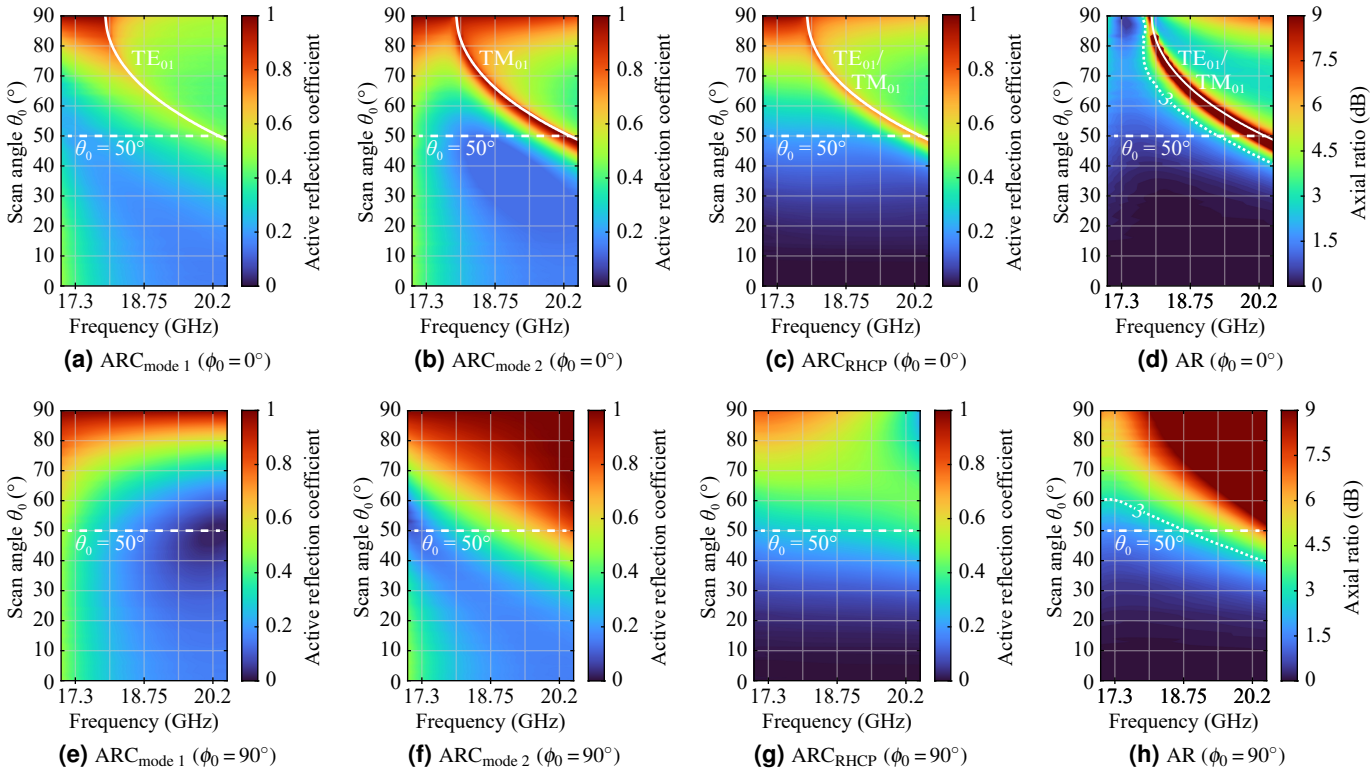

Figure 8: ARCs in a linear scale and AR in dB as functions of frequency and scan angle of the H6RWG with an element periodicity of $0.65\lambda_{\text{min}}$ for $\phi_0 = 0°$ and 90°. The maximum scan angle, the 3 dB AR threshold, and the first two higher-order Floquet modes (TE$_{01}$ and TM$_{01}$) in the $\phi_0 = 0°$-plane are indicated in white dashed, dotted, and solid lines, respectively.

limitations. Nevertheless, similar observations also result from the other previously discussed configurations.

The fundamental waveguide modes play a crucial role in explaining the scan limitations. In Fig. 7, the field distributions of the two fundamental waveguide modes of the H6RWG are illustrated. The ARCs of the fundamental waveguide modes can be defined as

$$\text{ARC}_{\text{mode 1}} = \text{S}_{11} + j \cdot \text{S}_{12} \tag{8}$$

$$\text{ARC}_{\text{mode 2}} = \text{S}_{22} - j \cdot \text{S}_{21}\,, \tag{9}$$

assuming an ideal RHCP excitation.

Fig. 8 shows the ARCs of the two fundamental waveguide modes at the excited port of the polarizer (RHCP) on a linear scale and the AR in dB versus the scan angle θ_0 and frequency for $\phi_0 = 0°$ and $\phi_0 = 90°$. A linear scale is chosen to capture the full dynamic range of the ARCs.

When scanning in the $\phi_0 = 0°$-plane, there are pairs of frequency / scan angle conditions where the ARC associated with waveguide mode 2 is unity. Under the same conditions, the AR is much higher than 9 dB. From phased array theory, it is known that in an infinite array, a total reflection condition with a corresponding zero in the active element pattern, called scan blindness, may occur at the frequency and scan angle at which higher-order Floquet modes begin to propagate. At this frequency and angle, an end-fire grating lobe appears. In Fig. 8(a)-(d), a white line indicates these frequency / scan angle pairs corresponding to the excitation of these higher-order Floquet modes (TE$_{01}$ and TM$_{01}$). When scanning in the $\phi_0 = 90°$-plane (bottom graphs in Fig. 8), the behavior is different because higher-order Floquet modes do not propagate in the considered frequency band. Nevertheless, a continuous degradation of the ARC of waveguide mode 2 and of the AR can be observed.

2.2.1. Modal Analysis

To further investigate these scan limitations, a Floquet mode analysis is performed in the following. Fig. 9(a), (b), (d), and (e) show the transmission coefficients between the fundamental waveguide modes (denoted as waveguide modes 1/2) and the fundamental and first four higher-order Floquet modes (denoted as TE$_{00}$, TM$_{00}$, TE$_{01}$, TM$_{01}$, TE$_{-10}$, and TM$_{-10}$) for scanning in the $\phi_0 = 0°$- and 90°-plane. The phase constants of the fundamental and first three higher-order waveguide modes (denoted as waveguide modes 3/4 and 5), as well as those of the Floquet modes, are plotted in Fig. 9(c) and (f) for scanning in the same planes. Thereby, the phase constant β corresponds to the imaginary part of the propagation constant, which is defined as

$$\gamma = \alpha + j \cdot \beta\,, \tag{10}$$

with α as the attenuation constant.

For $\phi_0 = 0°$, prior to the onset of the higher-order Floquet modes (TE$_{01}$ and TM$_{01}$), indicated by their cut-off frequencies, a transmission zero occurs for waveguide mode 2 with respect to the TM$_{00}$ Floquet mode, as also observed in Fig. 8(b) for the ARC of waveguide mode 2. Therefore, waveguide mode 2 does

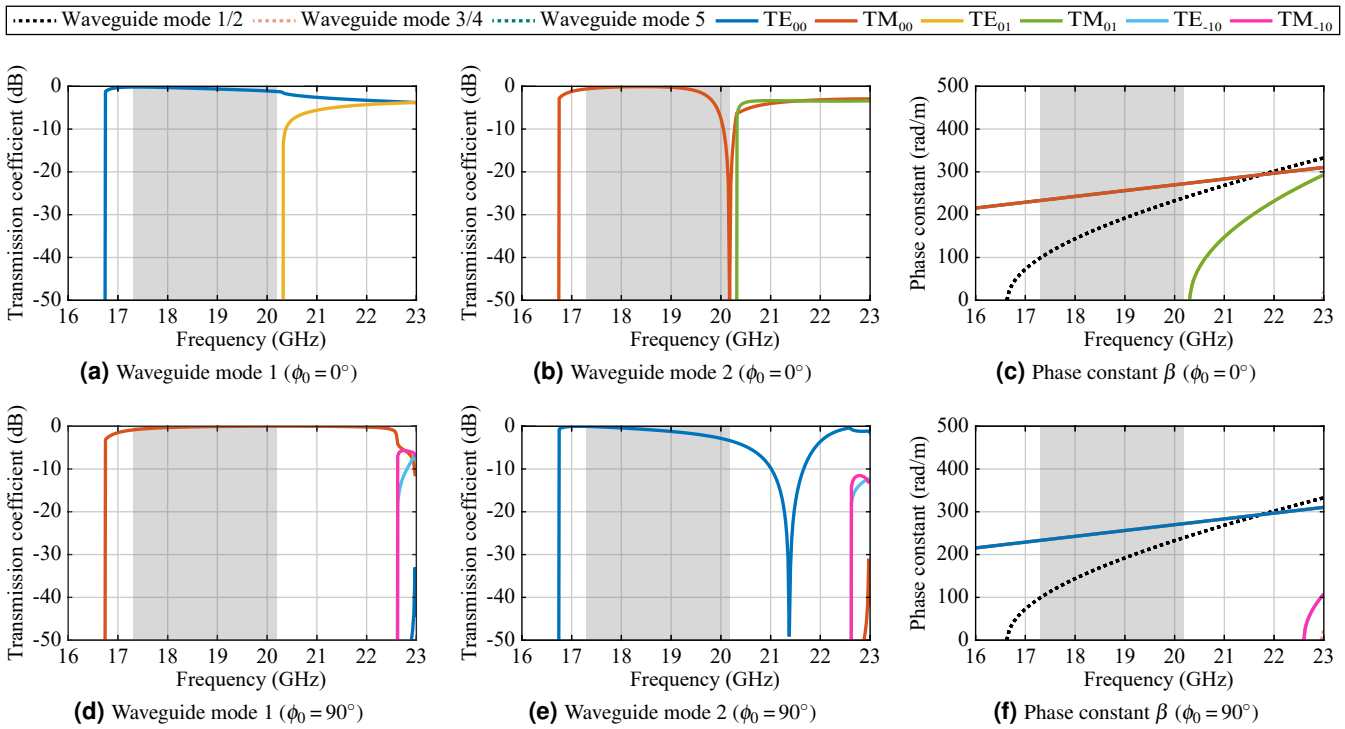

Figure 9: Floquet mode transmission coefficients and phase constants of the fundamental and the first four higher-order waveguide and Floquet modes of the H6RWG with an element periodicity of $0.65\lambda_{\text{min}}$ for $\phi_0 = 0°$ and 90° at $\theta_0 = 50°$. Not shown modes are not excited in the shown frequency range. The considered operational band is highlighted in light gray.

not contribute to the array radiation at this frequency. Instead, the transmission between waveguide mode 1 and the fundamental Floquet mode TE_{00} is not affected by such a transmission zero. An unequal contribution of the two orthogonal modes to the circularly polarized radiated field results in the observed strong degradation of the AR. As expected, for frequencies above the cut-off of the higher-order Floquet modes, half of the power of the waveguide modes is coupled to the respective first higher-order Floquet modes.

When scanning in the $\phi_0 = 90°$-plane, a transmission zero of waveguide mode 2 can also be observed. Because the waveguide modes are spatially orthogonal, the coupling to the fundamental Floquet modes switches between the $\phi_0 = 0°$ and $\phi_0 = 90°$ planes, and the TE_{00} Floquet mode is affected.

However, in contrast to the $\phi_0 = 0°$-plane, the transmission zero is observed much earlier than the onset of the higher-order Floquet modes (TE_{-10} and TM_{-10}). The transmission zero occurs close to the frequency where the phase constants of the fundamental waveguide modes match those of the fundamental Floquet modes. Under this condition, it is interpreted that the structure supports surface waves, and most of the power of waveguide mode 2 is not radiated. Although the transmission zero occurs at a frequency much higher than the maximum operational frequency, a slowly increasing attenuation is already observed within the considered band. This corresponds to a degradation of the AR with frequency, as seen in Fig. 8(h).

2.2.2. Role of the Element Periodicity

It is well-known that the onset of higher-order Floquet modes can be delayed by reducing the element periodicity. Since a reduction in the element periodicity translates into a reduction of the waveguide size, the cut-off frequencies are also modulated. In Fig. 10, the fundamental (denoted as waveguide modes 1/2) and first two higher-order waveguide mode (denoted as waveguide modes 3/4) cut-off frequencies, as well as the ridge height, are shown as functions of the element periodicity for the H6RWG, while maintaining a fundamental mode cut-off fre-

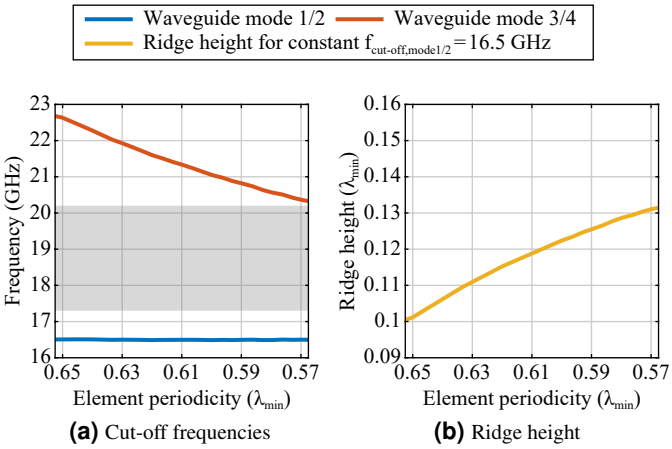

Figure 10: Fundamental (denoted as waveguide modes 1/2) and first two higher-order waveguide mode (denoted as waveguide modes 3/4) cut-off frequencies, as well as ridge height, as functions of the element periodicity for the H6RWG, while maintaining fundamental waveguide mode cut-off frequencies ($f_{\text{cut-off,mode1/2}}$) of 16.5 GHz.

quency of 16.5 GHz. As the element periodicity decreases, the cut-off frequencies of the higher-order waveguide modes also decrease, resulting in a reduced fundamental mode bandwidth.

In the following, two reduced element periodicities are considered: an intermediate element periodicity of $0.61\lambda_{\text{min}}$ (≈ 9.05 mm), and the maximum completely grating lobe free el-

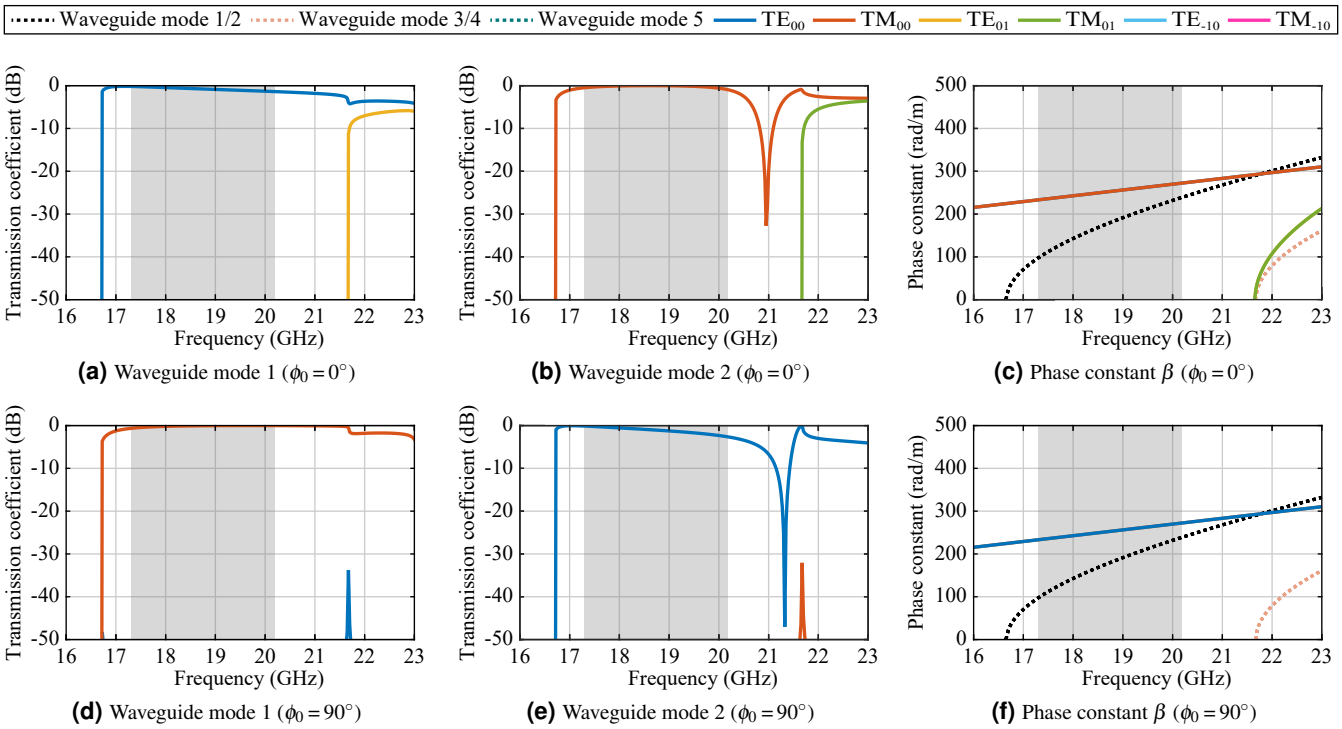

(a) Waveguide mode 1 ($\phi_0 = 0°$) **(b)** Waveguide mode 2 ($\phi_0 = 0°$) **(c)** Phase constant β ($\phi_0 = 0°$)

(d) Waveguide mode 1 ($\phi_0 = 90°$) **(e)** Waveguide mode 2 ($\phi_0 = 90°$) **(f)** Phase constant β ($\phi_0 = 90°$)

Figure 11: Floquet mode transmission coefficients and phase constants of the fundamental and the first four higher-order waveguide and Floquet modes of the H6RWG with an element periodicity of $0.61\lambda_{\text{min}}$ (≈ 9.05 mm) for $\phi_0 = 0°$ and 90° at $\theta_0 = 50°$.

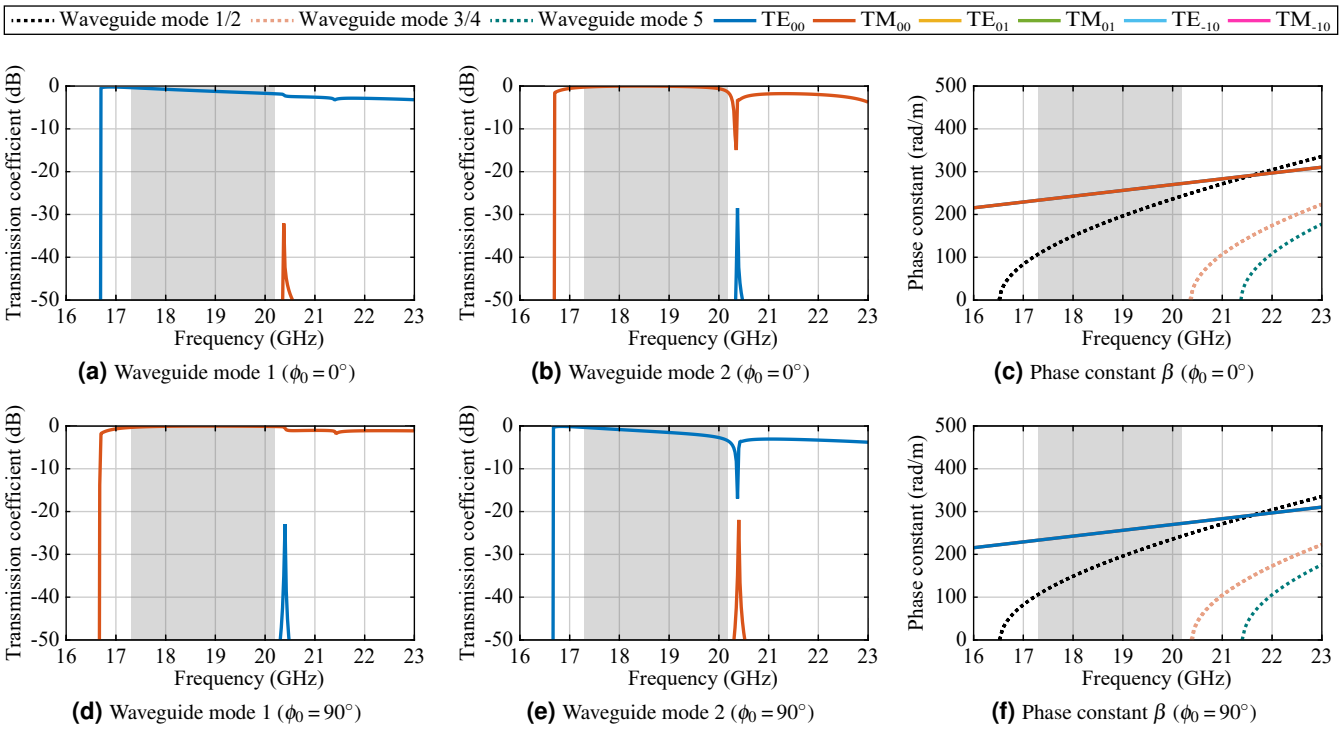

(a) Waveguide mode 1 ($\phi_0 = 0°$) **(b)** Waveguide mode 2 ($\phi_0 = 0°$) **(c)** Phase constant β ($\phi_0 = 0°$)

(d) Waveguide mode 1 ($\phi_0 = 90°$) **(e)** Waveguide mode 2 ($\phi_0 = 90°$) **(f)** Phase constant β ($\phi_0 = 90°$)

Figure 12: Floquet mode transmission coefficients and phase constants of the fundamental and the first four higher-order waveguide and Floquet modes of the H6RWG with an element periodicity of $0.57\lambda_{\text{min}}$ (≈ 8.45 mm) for $\phi_0 = 0°$ and 90° at $\theta_0 = 50°$.

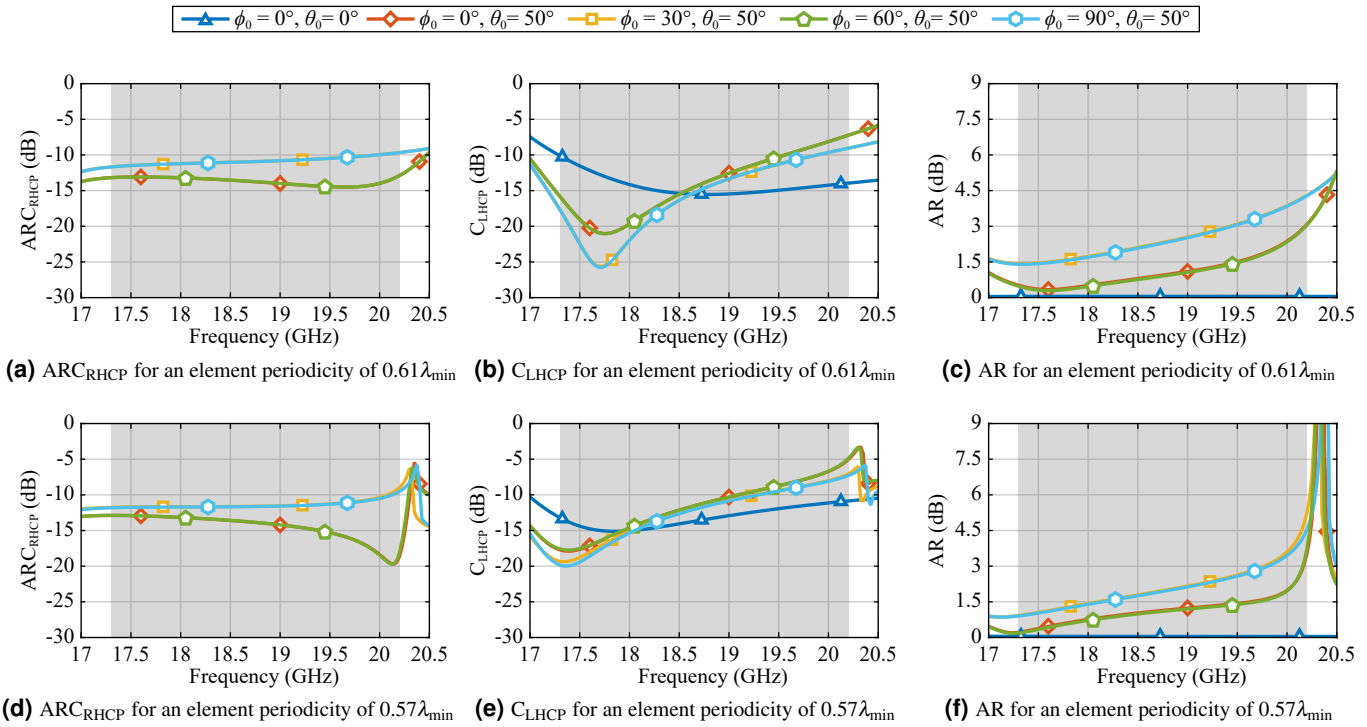

(a) ARC$_{RHCP}$ for an element periodicity of $0.61\lambda_{min}$ **(b)** C$_{LHCP}$ for an element periodicity of $0.61\lambda_{min}$ **(c)** AR for an element periodicity of $0.61\lambda_{min}$

(d) ARC$_{RHCP}$ for an element periodicity of $0.57\lambda_{min}$ **(e)** C$_{LHCP}$ for an element periodicity of $0.57\lambda_{min}$ **(f)** AR for an element periodicity of $0.57\lambda_{min}$

Figure 13: ARC, coupling coefficient, and AR as functions of frequency of the H6RWG with reduced element periodicities at the broadside and at the maximum scan angle of $\theta_0 = 50°$ for $\phi_0 = 0°$, 30°, 60°, and 90°. The ridge dimensions are set accordingly for identical fundamental waveguide mode cut-off frequencies of 16.5 GHz. Some curves are hidden under others due to symmetry.

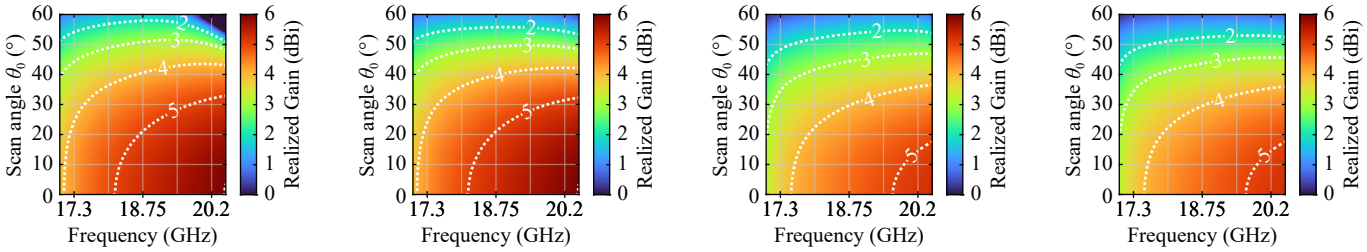

(a) H6RWG with an element periodicity of $0.61\lambda_{min}$ ($\phi_0 = 0°$) **(b)** H6RWG with an element periodicity of $0.61\lambda_{min}$ ($\phi_0 = 90°$) **(c)** H6RWG with an element periodicity of $0.57\lambda_{min}$ ($\phi_0 = 0°$) **(d)** H6RWG with an element periodicity of $0.57\lambda_{min}$ ($\phi_0 = 90°$)

Figure 14: Co-polarized (RHCP) realized gain as a function of frequency and scan angle of the H6RWG with an element periodicity of $0.61\lambda_{min}$ and $0.57\lambda_{min}$ for $\phi_0 = 0°$ and 90°.

Table 2: Summary of the scan limitations of the H6RWG with reduced element periodicites.

Aperture	Element periodicity	ARC$_{RHCP}$	C$_{LHCP}$	AR	G$^{max}_{RHCP}$	Scan loss
H6RWG	$0.61\lambda_{min}$	$\leq$ -9.7 dB	$\leq$ -7.2 dB	$\leq$ 4.3 dB	4.4 – 5.9 dBi	$\leq$ 3.1 dB
H6RWG	$0.57\lambda_{min}$	$\leq$ -9 dB	$\leq$ -4.8 dB	$\leq$ 5.2 dB	3.8 – 5.2 dBi	$\leq$ 2.7 dB

ement periodicity in a triangular lattice of $0.57\lambda_{min}$ (≈ 8.45 mm). Fig. 11 and Fig. 12 show the transmission coefficients and phase constants of the fundamental and higher-order waveguide and Floquet modes for the two reduced element periodicities, respectively.

For an element periodicity of $0.61\lambda_{min}$, the onset of higher-order Floquet modes is delayed by about 1.4 GHz, resulting in a transmission zero far out of band. However, the transmission zero occurs slightly earlier, at around 21 GHz, and can be attributed to the combined effect of the onset of higher-order Floquet modes and the alignment of the phase constants between the fundamental waveguide and Floquet modes, both occurring nearly at the same frequency.

The transmission zero of the TE$_{00}$ Floquet mode in the

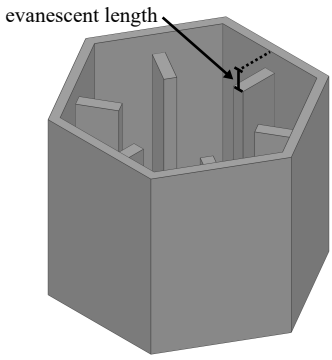

Figure 15: H6RWG aperture with an electrically short evanescent waveguide end-section.

$\phi_0 = 90°$-plane remains as the fundamental mode cut-off frequencies are maintained. Thus, the frequency at which the phase constants of the fundamental waveguide modes match those of the fundamental Floquet modes is the same. However, compared to an element periodicity of $0.65\lambda_{\min}$, the attenuation at the maximum operational frequency is slightly reduced for the TE_{00} Floquet mode. At the cut-off frequencies of the higher-order waveguide modes, slight modal coupling between the fundamental Floquet modes can be observed. In addition, the transmission coefficients begin to decrease at higher frequencies.

A further reduction of the element periodicity to $0.57\lambda_{\min}$ completely removes the propagation condition of higher-order Floquet modes at the maximum scan condition of $\theta_0 = 50°$ in the band. For waveguide mode 2, transmission zeros appear at the onset of the first two higher-order waveguide modes near the maximum operational frequency in both ϕ_0-planes, leading to increased attenuation at the maximum operational frequency. The transmission zeros arise from modal coupling between the fundamental and the first two higher-order waveguide modes.

The ARC, coupling coefficient, and AR as functions of frequency corresponding to the reduced element periodicities are depicted in Fig. 13. For an element periodicity of $0.61\lambda_{\min}$, the ARC, coupling coefficient, and AR are notably improved at high frequencies. Nevertheless, the 3 dB AR requirement is still not met in all ϕ_0-planes. Similarly, for an element periodicity of $0.57\lambda_{\min}$, the ARC, coupling coefficient, and AR improve for most frequencies. However, resonances at the cut-off frequencies of the first two higher-order waveguide modes cause significant degradations at the maximum operating frequency. Consequently, the 3 dB AR requirement also cannot be met for an element periodicity of $0.57\lambda_{\min}$.

In Fig. 14, the co-polarized (RHCP) realized gain is shown as a function of frequency and scan angle θ_0 for $\phi_0 = 0°$ and $90°$ for the H6RWG with the reduced element periodicities. The maximum realized gain reduces accordingly with decreasing aperture size. For the $0.61\lambda_{\min}$ element, the realized gain peaks between 4.4 dBi and 5.9 dBi with frequency at broadside, while for the $0.57\lambda_{\min}$ element, the realized gain peaks between 3.8 dBi and 5.2 dBi. The scan losses for both reduced element periodicities are significantly lower than those of the H6RWG with an element periodicity of $0.65\lambda_{\min}$. Specifically, scan loss remains below 3.1 dB for the $0.61\lambda_{\min}$ element and below 2.7 dB for the $0.57\lambda_{\min}$ element.

Table 2 summarizes the scan limitations of the H6RWG with the reduced element periodicities.

3. Open-ended Ridged Waveguide Apertures with Evanescent End-Section

Open-ended ridged waveguides with evanescent waveguide sections have already been investigated in the literature [6, 7, 9], primarily to enhance bandwidth in active matching and coupling. Using an electrically short evanescent waveguide section at the aperture end allows to partly overcome the scan limitations of conventional open-ended ridged waveguide PAAs, as the waveguide mode cut-off frequencies are shifted to higher frequencies before radiation. Consequently, the frequency at which the phase constants of the fundamental waveguide modes match those of the fundamental Floquet modes is also shifted. Fig. 15 depicts the H6RWG aperture with an electrically short evanescent waveguide end-section. Since an evanescent wave-

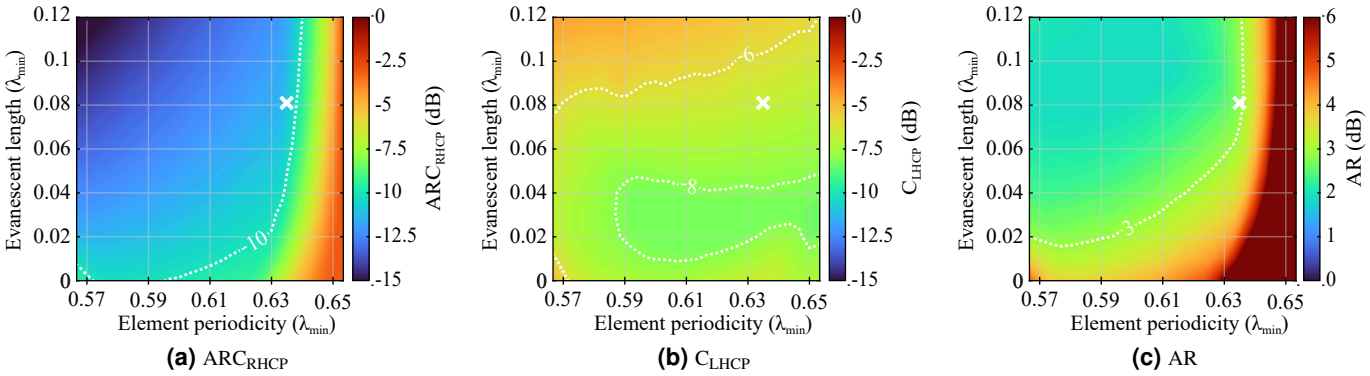

(a) ARC_{RHCP} **(b)** C_{LHCP} **(c)** AR

Figure 16: Maximum ARC, coupling coefficient, and AR evaluated within the considered bandwidth and scan range for different evanescent lengths and element periodicities. The ridge dimensions are set for constant fundamental waveguide mode cut-off frequencies of 16.5 GHz. A white cross marks the maximum usable element periodicity of $0.635\lambda_{\min}$ (≈ 9.425 mm) for an AR of less than 3 dB while minimizing the ARC and coupling coefficient.

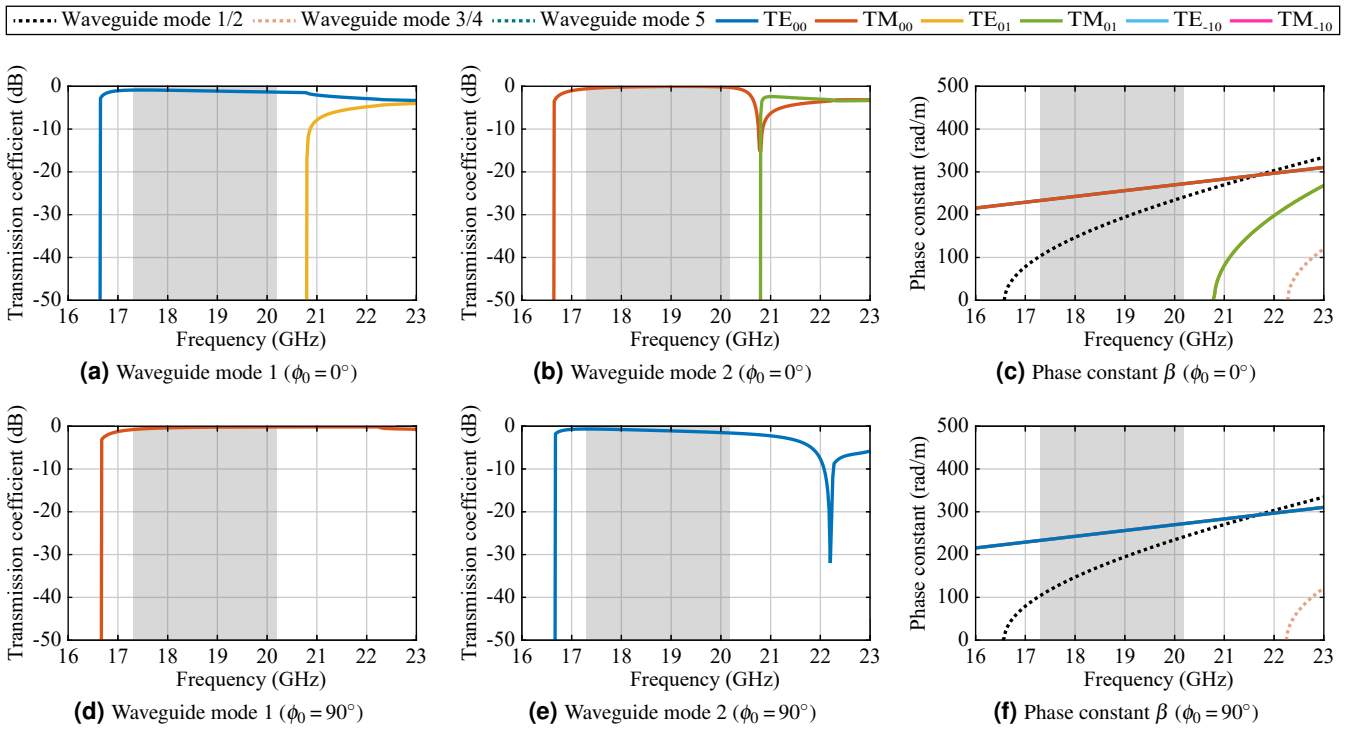

Figure 17: Floquet mode transmission coefficients and phase constants of the fundamental and the first two higher-order waveguide and Floquet modes of the H6RWG with an element periodicity of $0.635\lambda_{\text{min}}$ and an evanescent waveguide end-section length of about $0.081\lambda_{\text{min}}$ (≈ 1.2 mm) for $\phi_0 = 0°$ and 90° at $\theta_0 = 50°$. Not shown modes are not excited in the shown frequency range.

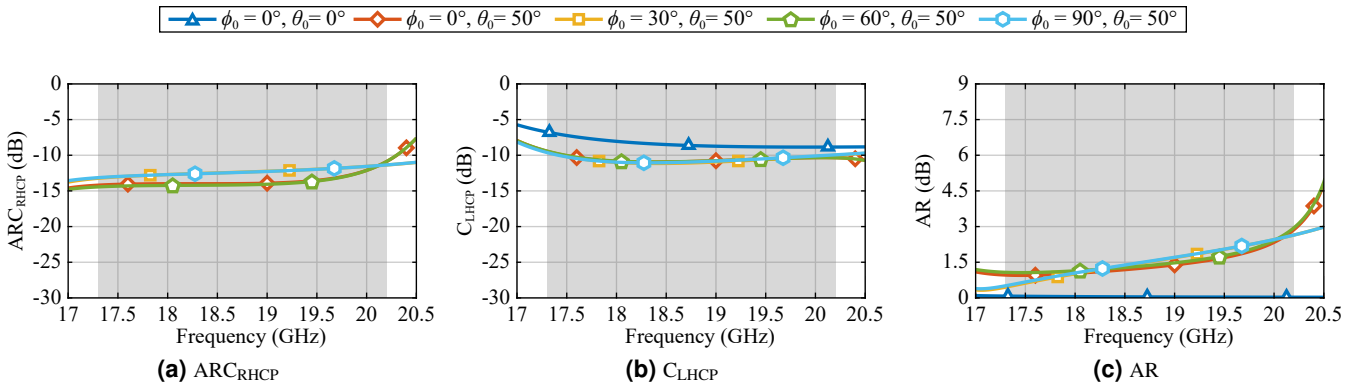

Figure 18: ARC, coupling coefficient, and AR as functions of frequency of the H6RWG with an element periodicity of $0.635\lambda_{\text{min}}$ and an evanescent waveguide end-section length of about $0.081\lambda_{\text{min}}$ at the broadside and at the maximum scan angle of $\theta_0 = 50°$ for $\phi_0 = 0°$, 30°, 60°, and 90°. Some curves are hidden under others due to symmetry. The considered operational band is highlighted in light gray.

guide section also affects the active matching and coupling, the length of the evanescent waveguide section must be carefully chosen, resulting in a trade-off between active matching, coupling, and AR.

In Fig. 16 the maximum ARC, coupling coefficient and AR are evaluated within the considered bandwidth and scan range for different evanescent lengths and element periodicities. The ridge dimensions are set accordingly for constant fundamental waveguide mode cut-off frequencies of 16.5 GHz. For an element periodicity of $0.57\lambda_{\text{min}}$, the 3 dB AR can be achieved when an electrically short evanescent length of $0.02\lambda_{\text{min}}$ (≈ 0.3 mm) or more is used. Even for larger element periodicities, the AR remains below 3 dB as the evanescent length increases. However, saturation can be observed for element periodicities larger than $0.635\lambda_{\text{min}}$ (≈ 9.425 mm). This can be explained by the onset of higher-order Floquet modes. A white cross in Fig. 16 marks the maximum usable element periodicity for an AR of less than 3 dB while minimizing the ARC and the coupling coefficient. The corresponding evanescent length is about $0.081\lambda_{\text{min}}$ (≈ 1.2 mm). Increasing the evanescent length further would only degrade the coupling coefficient.

Fig. 17 shows the transmission coefficients and phase con-

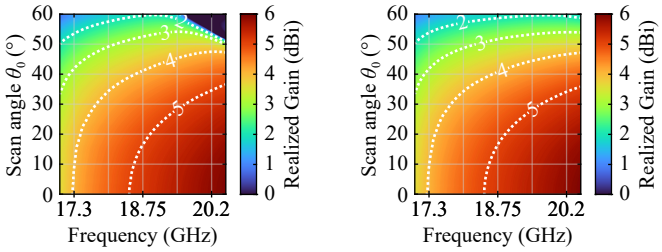

Figure 19: Co-polarized (RHCP) realized gain as a function of frequency and scan angle of the H6RWG with an element periodicity of $0.635\lambda_{min}$ and an evanescent waveguide end-section length $0.081\lambda_{min}$ for $\phi_0 = 0°$ and 90°.

stants of the fundamental and the first two higher-order waveguide and Floquet modes of the H6RWG with an element periodicity of $0.635\lambda_{min}$ and an evanescent waveguide end-section length $0.081\lambda_{min}$. As expected, for $\phi_0 = 0°$, a transmission zero of waveguide mode 2 appears before the onset of the TM_{01} Floquet mode. A further increase of the element periodicity would shift this transmission zero closer to the maximum operational frequency, leading to increased attenuation, and consequently, degradation of the AR. For $\phi_0 = 90°$, the transmission zero of waveguide mode 2 is shifted to higher frequencies, reducing the attenuation of the TE_{00} Floquet mode in the operational frequency band.

Furthermore, Fig. 18 shows the ARC, the coupling coefficient, and the AR as functions of frequency of the selected H6RWG with an evanescent waveguide end-section for different scan directions. The ARC, coupling coefficient, and AR are smaller than -10.5 dB, -6.8 dB, and 3 dB, respectively.

In Fig. 19, the co-polarized (RHCP) realized gain is shown as a function of frequency and scan angle θ_0 for $\phi_0 = 0°$ and 90°. The realized gain peaks between 4.1 and 5.9 dBi with frequency at broadside and degrades up to 2.3 dB when scanned to the maximum scan angle of $\theta_0 = 50°$. However, compared to the H6RWG with an element periodicity of $0.61\lambda_{min}$, a slight degradation can be observed in the peak realized gain at low frequencies.

4. Conclusions

In this paper, the scan limitations of open-ended circular and hexagonal waveguide PAA elements with three and six ridges have been discussed. Strong degradation in ARC, coupling to the terminated (cross-polarized) port of the polarizer, AR and realized gain was observed for all analyzed elements when using the maximum grating lobe free (with respect to the considered operational frequency band) element periodicity of $0.65\lambda_{min}$ for scanning up to $\theta_0 = 50°$. For the H6RWG, the scan limitations have been thoroughly investigated for different element periodicities by analyzing the individual contribution of the two fundamental waveguide modes to the array radiation. The degradations can be related to three conditions. First, the onset of higher-order Floquet modes at the edge of the operating frequency band leads to single-mode scan blindness associated with one of the two orthogonal fundamental waveguide modes. Second, the matching of the phase constants of the fundamental waveguide modes and the fundamental Floquet modes far outside the operational band is interpreted as being associated with surface wave propagation and results in an increased attenuation at the maximum operational frequency. Third, the onset of higher-order waveguide modes causes modal coupling between the fundamental and the first two higher-order waveguide modes. Each of these conditions results in unequal contributions from the two fundamental waveguide modes to the radiated field, thereby degrading the overall performance. However, the scan limitations are determined solely by the first condition that is met, and any other condition that may also be fulfilled at a higher frequency has no additional impact within the considered operating band. Apart from the third condition, which does not affect three-ridged waveguides due to their large fundamental mode bandwidth, similar observations will also result for the C3RWG, C6RWG, and H3RWG.

Table 3: Comparison of similar apertures from the literature for scan angles up to $\theta_0 = 50°$.

Aperture	Lattice	Element periodicity	Relative bandwidth	ARC_{RHCP}	C_{LHCP}	AR	G^{max}_{RHCP}	Scan loss
S4RWG[1] with multiple evanescent sections [5]	□	$0.55\lambda_{min}$[2]	5%	≤ -10 dB	≤ -6 dB	≤ 7.3 dB[2]	3.5 – 5 dBi	≤ 2.7 dB
S4RWG[1] with evanescent end-section [9]	□	$0.526\lambda_{min}$[2]	13.2%	≤ -11 dB	≤ -4 dB	≤ 3.5 dB[2]	not reported	≤ 2 dB
H3RWG [9]	△	$0.606\lambda_{min}$[2]	13.2%	≤ -11 dB	≤ -6 dB	≤ 5 dB[2]	not reported	≤ 3 dB
H6RWG [9]	△	$0.606\lambda_{min}$[2]	13.2%	≤ -10 dB	≤ -8 dB	≤ 4.5 dB[2]	not reported	≤ 3 dB
H6RWG cascaded with a septum polarizer [10]	△	$0.633\lambda_{min}$	15.5%	≤ -7 dB	≤ -7.8 dB	≤ 12.2 dB[3]	4.5 – 5.9 dBi	≤ 5.3 dB[3]
H6RWG with evanescent end-section (**This work**)	△	$0.635\lambda_{min}$	15.5%	≤ -10.5 dB	≤ -6.8 dB	≤ 3 dB	4.1 – 5.9 dBi	≤ 2.3 dB

[1] Square 4-ridged waveguide (S4RWG), also known as quad-ridged waveguide. [2] Calculated from reported data. [3] Added by the author.

By introducing an electrically short evanescent section at the end of the aperture, the scan limitations can be overcome for element periodicities up to $0.635\lambda_{\min}$, meeting the 3 dB AR requirement. The evanescent end section modifies the waveguide propagation characteristics by increasing the cut-off frequencies before radiation, thereby addressing the second and third condition.

Table 3 compares the performance of the H6RWG with an electrically short evanescent waveguide end-section with an element periodicity of $0.635\lambda_{\min}$ with similar ridged waveguide apertures reported in the literature in an infinite array environment. With the exception of the aperture presented in [10], all other apertures are also evaluated using an ideal polarizer. The widest relative bandwidth is achieved with an ARC of less than -10 dB and an AR of less than 3 dB. Furthermore, the realized gain peaks between 4.1 dBi and 5.9 dBi with frequency at broadside with scan losses of less than 2.3 dB at $\theta_0 = 50°$. However, the coupling coefficient remains relatively high ($\geq$ -10 dB), a problem common to all compared apertures.

For the H6RWG with an electrically short evanescent end-section, an improvement of up to 2 dB for the coupling coefficient can be achieved if smaller element periodicities can be tolerated. Lower coupling coefficients can also be achieved by optimizing the ridge heights or by using multiple evanescent waveguide sections, as reported in [5] and [8]. To achieve even larger element periodicities, the choked [6] and slotted horn apertures [10] are promising solutions and will be part of future investigations.

Acknowledgment

Funded by the European Union, under ANTERRA 101072363 HORIZON-MSCA-2021-DN-01. Views and opinions expressed are however those of the author(s) only and do not necessarily reflect those of the European Union. Neither the European Union nor the granting authority can be held responsible for them.

References

[1] M. Giordani and M. Zorzi, "Non-terrestrial networks in the 6g era: challenges and opportunities," *IEEE Network*, vol. 35, no. 2, pp. 244–251, 2021.

[2] X. Lin, S. Cioni, G. Charbit, N. Chuberre, S. Hellsten and J. -F. Boutillon, "On the path to 6g: embracing the next wave of low earth orbit satellite access," *IEEE Communications Magazine*, vol. 59, no. 12, pp. 36–42, 2021.

[3] H. Shahid *et al*, "Emerging advancements in 6g ntn radio access technologies: an overview," *2024 Joint European Conference on Networks and Communications & 6G Summit (EuCNC/6G Summit)*, pp. 593–598, 2024.

[4] A. K. Bhattacharyya, "Phased array antennas: floquet analysis, synthesis, bfns and active array systems," *Wiley Series in Microwave and Optical Engineering*, Chapter 8, 2006.

[5] L. Polo-López, E. Menargues, S. Capdevila, G. Toso and M. García-Vigueras, "Solving sub-wavelength lattice reduction in full-metal front-ends for dual-polarized active antennas," *IEEE Transactions on Antennas and Propagation*, vol. 70, no. 9, pp. 7413-7426, 2022.

[6] D. Pla *et al*, "High efficiency and circular polarization in satcom phased arrays using tri-ridge apertures," *Scientific Reports*, vol. 14, no. 20285, 2024.

[7] E. Menargues, S. Capdevila, M. Vizcarro, M. Billod, I. Bengocchea and M. García-Vigueras, "Metal 3d-printed high-performance radiating panel for satcom aesa terminals," *2024 IEEE International Symposium on Phased Array Systems and Technology (ARRAY)*, Boston, MA, USA, pp. 1-5, 2024.

[8] L. Polo-López, L. Berretti, E. Menargues, S. Capdevila, G. Toso and M. García-Vigueras, "Dual-polarized spaceborne phased arrays using tri-ridge evanescent waveguide antennas," *IEEE Antennas and Wireless Propagation Letters*, vol. 24, no. 3, pp. 656-660, 2025.

[9] C. Vazquez-Sogorb, R. Montoya-Roca, G. Addamo, O. A. Peverini and G. Virone, "Ridged apertures for leo direct radiating arrays in ka-band," *Applied Sciences*, vol. 14, no. 17, pp. 272–275, 2024.

[10] S. Harms *et al*, "Waveguide antenna array element with minimized power amplifier load pull for leo ntns," *2024 54th European Microwave Conference (EuMC)*, Paris, France, pp. 272-275, 2024.

[11] S. Harms, J. -P. Fraysse, S. Monni, A. Garufo and U. Johannsen, "Scan limitations of open-ended ridged waveguide phased array antennas for satellite communication," *2025 19th European Conference on Antennas and Propagation (EuCAP)*, Stockholm, Sweden, pp. 1-5, 2025.

[12] A. I. Dimitriadis, M. Favre, M. Billod, J. -P. Ansermet and E. de Rijk, "Design and fabrication of a lightweight additive-manufactured ka-band horn antenna array," *10th European Conference on Antennas and Propagation (EuCAP)*, Davos, Switzerland, pp. 1–4, 2006 .

[13] L. Berretti, L. Polo-Lopez, E. Menargues, R. Loison, G. Toso and M. García-Vigueras, "The role of additive manufacturing in space-borne active antenna," *2023 17th European Conference on Antennas and Propagation (EuCAP)*, Florence, Italy, pp. 1-4, 2023.

[14] E. García-Marín, J. L. Masa-Campos, P. Sánchez-Olivares and J. A. Ruiz-Cruz, "Evaluation of additive manufacturing techniques applied to ku-band multilayer corporate waveguide antennas," *IEEE Antennas and Wireless Propagation Letters*, vol. 17, no. 11, pp. 2114-2118, 2018.

[15] O. A. Peverini, M. Lumia, G. Addamo, G. Virone and N. J. G. Fonseca, "How 3d-printing is changing rf front-end design for space applications," *IEEE Journal of Microwaves*, vol. 3, no. 2, pp. 800-814, 2023.

[16] Ansys Inc, Ansys HFSS - 3D High Frequency Electromagnetic Field Simulator, *[Online]. Available: https://www.ansys.com/products/electronics/ansys-hfss*, Accessed: 2025.

[17] C. A. Balanis, "Antenna Theory: Analysis and Design, 4th edition," *Wiley*, Chapter 2, 2016.